objects (Fig. 3a) are ruby crystals, whose high relief is caused by their high refractive index relative to the surrounding hydrogen crystals. The gray-toned crystals (Fig. 3b) are the high-pressure phase, surrounded at the crystal margins with the light-colored, low-pressure liquid at this transition point. Relief along the boundaries is the Becke line, indicating that the high-pressure phase is considerably denser than the low-pressure phase.

As the pressure was increased above 57 kbar, the low-pressure phase disappeared, and the high-pressure phase became compressed and its refractive index increased. The ruby crystals became clear, and the visible boundary line between ruby and high-pressure hydrogen crystals disappeared at 360 kbar (Fig. 3c). Thus, the refractive indexes of the two materials had become the same. Accordingly, the results of calculations indicate that the density of the high-pressure hydrogen crystals had increased. The crystals were colorless at first, but they appeared to obtain a yellowish tint in some parts of the cell. A calculation of the specific gravity based on estimates of the average refractive index of this high-pressure phase gives 0.6 to 0.7 at 360 kbar. Between 360 and 500 kbar, no further changes were noted, except perhaps a slight darkening of the yellow color and a continuous increase in the index of refraction of the hydrogen phase relative to ruby.

The solidification is not observed to have the type of hysteresis associated with order-disorder transformations due to varying proportions of the ortho and para spin states of molecular hydrogen (*6*). Nevertheless, it is probable that both of these phases of hydrogen contain a mixture of states, possibly disordered.

Implications. The solidification point (57 kbar) observed at room temperature in this study is very close to that predicted (*7*). The room-temperature solid phase observed to 500 kbar in this study is not related to the known, complex, low-temperature structural transformations in hydrogen and does not appear to change at approximately 120 kbar, which was calculated for the transformation (*6*).

The specific-gravity value of 0.6 to 0.7 for the high-pressure phase at 360 kbar agrees within the uncertainty with the values for generalized models of solid hydrogen calculated from theory by Liberman (*8*) and Ross and Shishkevish (*1*).

There is no direct evidence in the present experiments on which to base a choice of the physical process by which hydrogen will become (i) conducting in the molecular state or (ii) an atomic-like superconducting metal. A gradual, high order-type transition to the metallic state, similar to the metallic transition in iodine, could occur in hydrogen, and it has been stressed, for example, that measurements of electrical conductivity alone in high-pressure experiments with hydrogen are likely to be ambiguous (*1*).

The liquid and the new high-pressure phase of hydrogen are amenable to further characterization by measuring the Raman spectra, visible and near-infrared spectra, and electrical and magnetic properties. A separate set of experiments will be required for the generation of pressures on solid hydrogen above 500 kbar because of the nature of this technique (*2*). At present there is no reason to believe that pressures above 500 kbar on hydrogen cannot be achieved with the diamond-anvil, high-pressure apparatus.

H. K. MAO, P. M. BELL
Geophysical Laboratory, Carnegie Institution of Washington, Washington, D.C. 20008

References and Notes

1. A moderately complete review of theoretical models for the high-pressure behavior of hydrogen is given by M. Ross and C. Shishkevish, *Molecular and Metallic Hydrogen* (R-2056-ARPA, Rand Corporation, Santa Monica, Calif., 1977).
2. H. K. Mao and P. M. Bell, *Science* **200**, 1145 (1978).
3. The hydrogen gas used in these experiments was Linde ultrahigh purity grade (99.999 percent pure). It was piped by a liquid nitrogen trap through cleaned copper tubing with brass and stainless steel fittings. Evacuation cycles and continuous hydrogen purging (average rate, 0.5 liter/min) of the system were carried out repetitively up to the instant of filling the sample chamber. In the pressure cell, hydrogen was in contact with ruby, stainless steel, and diamond. No precipitates were observed on release of the pressure; the impurities in the hydrogen, therefore, were probably less than 0.01 percent. The ruby composition was laser grade Al_2O_3 plus 0.55 percent Cr by weight. Stainless steel was Ulbrich type 301, full hard, iron plus C (0.117 percent by weight), Mn (1.09), Si (0.49), P (0.026), S (0.011), Cr (16.93), Ni (7.35), Mo (0.31), Cu (0.23), and N (0.0370).
4. H. K. Mao, P. M. Bell, J. Shaner, D. Steinberg, *J. Appl. Phys.* **49**, 3276 (1978).
5. The image was recorded on a Panasonic time-lapse videotape recorder from a Hitachi CCTV unit.
6. R. L. Mills, *J. Low Temp. Phys.* **31**, 423 (1978).
7. D. H. Liebenberg, R. L. Mills, J. C. Bronson, *Phys. Rev. B* **18**, 4526 (1978).
8. D. A. Liberman, *Los Alamos Sci. Lab. Rep. LA-4727-MS* (1971).

30 January 1979

Mars Gravity: High-Resolution Results from Viking Orbiter 2

Abstract. *Doppler radio-tracking data have provided detailed measurements for a martian gravity map extending from 30°S to 65°N in latitude and through 360° of longitude. The feature resolution is approximately 500 kilometers, revealing a huge anomaly associated with Olympus Mons, a mascon in Isidis Planitia, and other anomalies correlated with volcanic structure. Olympus Mons has been modeled with a 600-kilometer surface disk having a mass of 8.7×10^{21} grams.*

On 25 October 1977, the periapsis altitude of the Viking Orbiter 2 spacecraft was lowered to 300 km. This event provided a unique opportunity for the acquisition of nearly global, detailed measurements of the martian gravity field. Earlier data had been acquired with the spacecraft at much higher altitudes where gravity effects were significantly attenuated and feature resolution was very limited. These analyses (*1–3*) revealed principally the regional Tharsis gravity high and flanking lows in the Chryse and Amazonis lowlands. Some investigators (*2*) determined the Hellas basin as a gravity low. Using a very limited set of data from Viking Orbiter 1 at a periapsis altitude of 300 km, Sjogren *et al.* (*4*) provided some corroborating results for Olympus Mons and Alba Patera; but the zone of maximum sensitivity is very narrow, and these results are overshadowed by the much greater detail and coverage of the Viking Orbiter 2 data.

The Viking Orbiter 2 data were obtained at a fortuitous time. A variety of problems had arisen in earlier observing periods: (i) the Earth-Mars distance was larger, and thus the return signals were weaker; (ii) the signal path was in closer proximity to the sun, and thus there was larger corruption by the solar plasma; (iii) occultation of the periapsis region occurred; and (iv) the periapsis altitude was larger. During the data collection from 25 October 1977 through March 1978, all of the above problems were eliminated and the line of sight from Earth was never more than 20° from the orbital plane of the spacecraft. This geometry allowed an almost direct measure of the vertical component of gravity; the periapsis altitude was between 270 to 300 km. The 80° orbital inclination of Viking 2 was another favorable factor, which made possible extensive coverage in latitude.

The requested tracking coverage was not obtained because of the many conflicting demands on the tracking station time. The resulting gaps in coverage are seen in Fig. 1, in which the near-vertical lines represent the locus of the spacecraft during the data taking. The Doppler signal was sampled every 10 seconds, which provided at least six Doppler data over a 300-km feature. The goal was to obtain orbital tracks every 4.5° or 270 km so that near-periapsis resolution could be uniformly preserved at the 300-to 500-km level. This data-acquisition strategy was based on the general empirical rule that the resolution of gravity features is approximately proportional to the spacecraft altitude. The data span for each arc is 1 hour before and 1 hour after periapsis (*5*). Since the spacecraft altitude is less than 1000 km for only 26 minutes, the high-resolution region near periapsis is well covered.

The data were reduced in two steps. The first step was a direct mapping of the line-of-sight (LOS) accelerations, in which I applied the same method as that used to map the lunar front-side gravity field (*6, 7*). In the second step, I selected orbital tracks over prominent gravity features (as determined in the first step) and estimated surface masses for those features using a least-squares filter on the Doppler data.

To produce the acceleration mapping, the raw Doppler observations were reduced with a large orbit determination program (*8*) that accounted for the major Doppler components such as the effects from solar and planetary perturbations, Earth rotation, and the orbital motion of the spacecraft. The martian gravity field model was held fixed with a 4th-degree and order model (*1*), and only the spacecraft position and velocity components were estimated (*9*). Each 2-hour arc of data was independently reduced to obtain Doppler residuals. Patched cubic splines were fitted in a least-squares sense to the Doppler residuals and were analytically differentiated to produce LOS accelerations. The accelerations were plotted as a function of the spacecraft latitude and longitude at the corresponding time. Contour lines were then inserted to produce a smooth map-

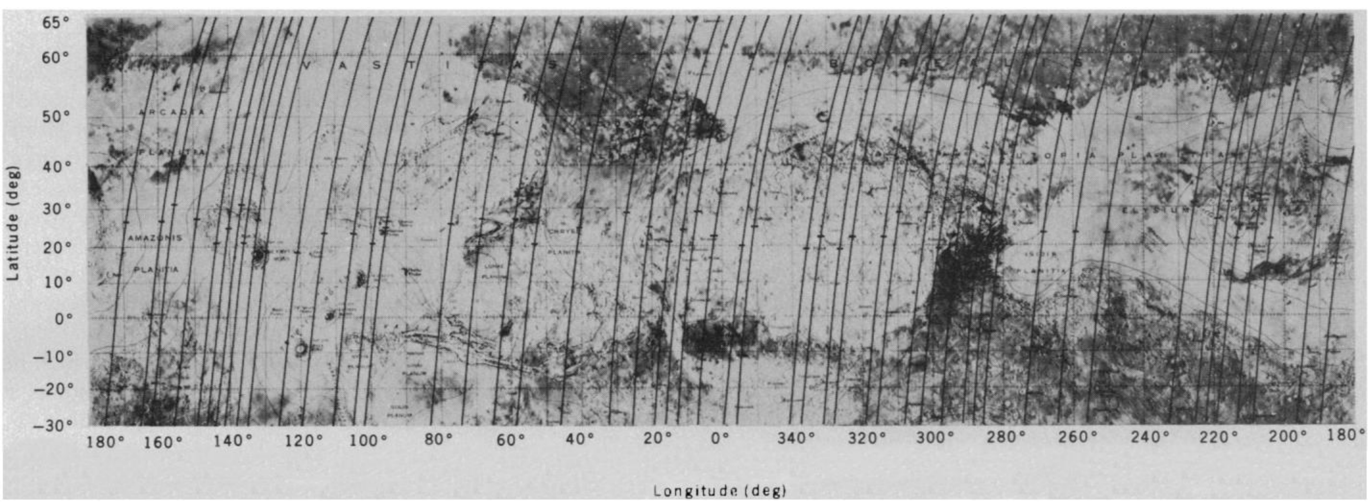

Fig. 1. Diagram of the data coverage. Lines represent the surface tracks of the Viking Orbiter 2 spacecraft during orbits of good Doppler data. The tick mark on each line indicates the periapsis location.

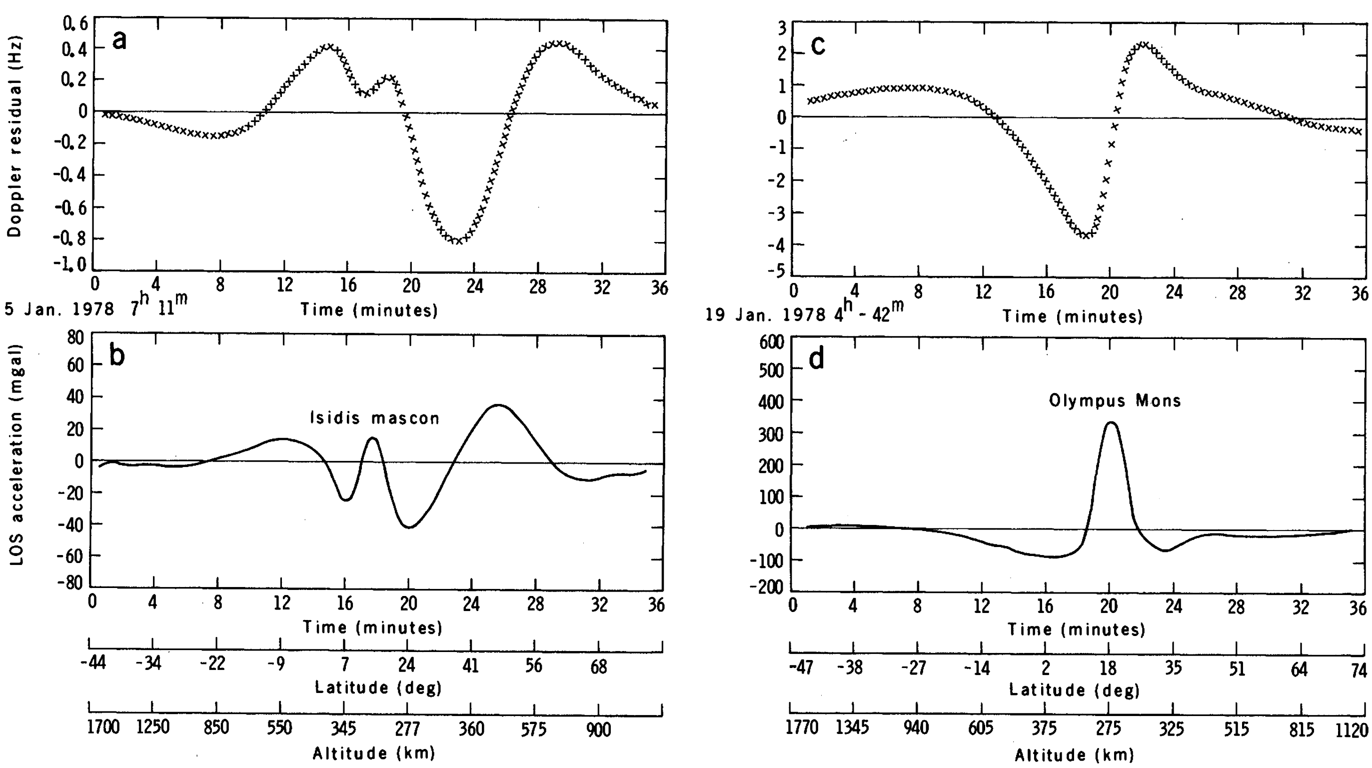

Fig. 2. Doppler residuals and LOS accelerations: (a) and (b) over Isidis Planitia; (c) and (d) over Olympus Mons; 1 Hz = 65 mm/sec.

Table 1. Mass estimates.

Feature	Latitude* (deg)	West longitude* (deg)	Disk radius* (km)	Mass† ($\times 10^{21}$ g)	Date
Olympus Mons	18.0	133.5	300	8.6	12 December 1977
Olympus Mons	18.0	133.5	300	8.8	19 January 1978
Alba Patera	40.5	109.0	450	2.8	14 December 1977
Arsia Mons	−9.0	120.5	180	2.3	28 February 1978
Elysium Mons	25.0	213.5	120	1.7	11 January 1978
Isidis mascon	12.0	271.0	240	0.8	5 January 1978

*Held fixed. †Estimated parameter.

ping over most of the northern hemisphere and part of the southern.

Examples of the Doppler residuals and LOS accelerations are shown in Fig. 2. The data noise level of 0.01 Hz is well below the systematic signatures. The Isidis and Olympus Mons anomalies are seen as prominent peaks that are derived from the steep gradients in the Doppler residuals plotted in Fig. 2, a and c, respectively. Periapsis was at 31°N latitude at the beginning of the data set and moved linearly southward to 17°N at the end. Since arcs are interspersed over several circulations (*10*) of the planet, adjacent profiles are not at precisely uniform altitudes and some averaging was applied in the final contouring.

Although the reduction method that was used preserves the high-frequency variations in the data, there are some adverse effects caused by the use of this approach. The primary effect is that the true amplitude of the peak anomalies (both positive and negative) may be reduced by 20 to 30 percent (*11*). Some small artificial anomaly values may be introduced on the sides of larger peaks. The orbital geometric effects also distort the sampling of the vertical gravity component. Thus, before the acceleration profiles are used for any quantitative estimates, these effects must be removed or accounted for. One should also remember that these accelerations are at spacecraft altitudes that vary ~ 500 km (Fig. 2) over the mapped zone.

The result of combining the LOS acceleration profiles into a gravity map is shown in Fig. 3. The correlation with topographic features is very evident. The most striking feature is Olympus Mons (18°N, 133°W), which is by far the largest gravity anomaly on Mars. It has a value of 344 mgal at a spacecraft altitude of 275 km. The largest anomaly detected on the moon was the Mare Serenitatis mascon, producing 246 mgal at 27-km altitude or 92 mgal at 120-km altitude (*12*). Since mascons are located in topographic depressions, their free-air gravity amplitudes are significantly reduced. In addition to the anomaly associated with the Olympus volcanic mountain, there is also a noticeable broadening in the anomaly to the northwest, which could possibly correspond to flows from Olympus Mons or a dense subsurface structure.

Alba Patera (40.5°N, 109°W), although not the most noticeable topographic feature (*13*), has a sizable gravity anomaly. This anomaly could also be an indication of a dense subsurface structure. The three volcanoes on the Tharsis ridge (≈ 110°W), Ascraeus Mons, Pavonis Mons, and Arsia Mons, have positive anomalies associated with them. The peak amplitudes of these anomalies were not obtained because tracking data were not acquired when the spacecraft passed directly over the features. There was an orbital track half way between Pavonis Mons and Arsia Mons that showed an anomaly encompassing both of these volcanoes. Arsia Mons and Ascraeus Mons stand out somewhat because they were also detected from orbits several degrees to the west and east, respectively (Fig. 1).

The Elysium Mons region (25°N, 213.5°W) is another volcanic area that has a well-defined anomaly. The anomaly is nearly centered over Elysium Mons but it is much broader than Elysium Mons itself, which suggests that an extensive subsurface structure may exist. Although there are orbital tracks near the Hecates volcano (32°N, 210°W), there does not appear to be an anomaly associated with it.

Isidis Planitia (12°N, 271°W), which is a topographic depression (*13*), contains a mascon (*14*). The entire surrounding region has a negative gravity anomaly, but in the midst of it there is a positive anomaly. Its relative amplitude is approximately 60 mgal, and it is comparable in size to the lunar mascons (*7*). This is the first such feature found on Mars, and it is most probably (*15*) the only one in the northern hemisphere.

The Valles Marineris structure lies in a gravity low. There is a minimum at the widening associated with Ophir Chasma,

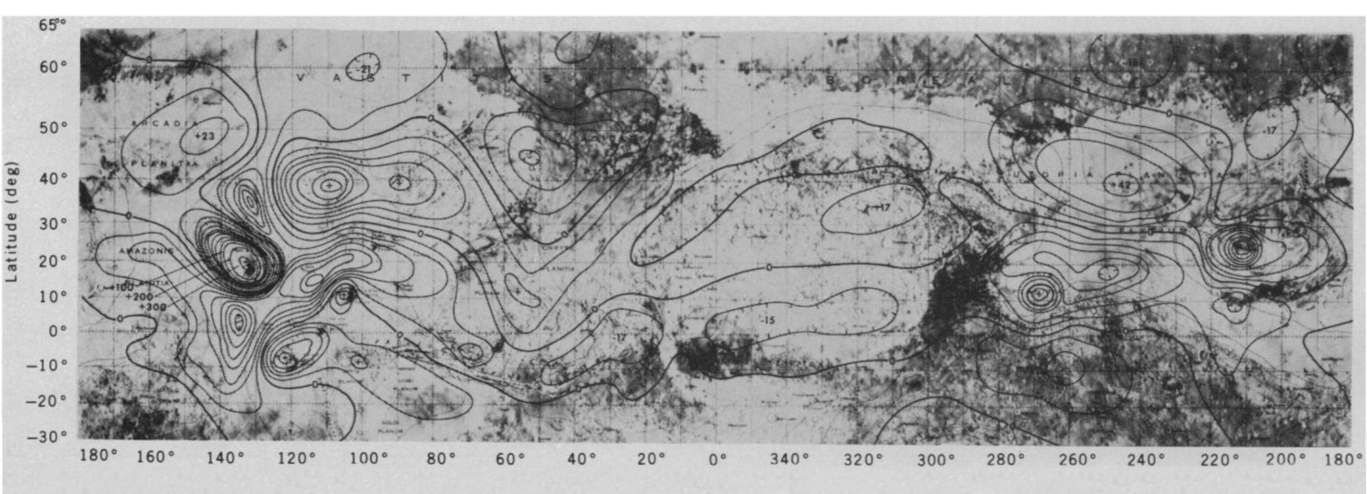

Fig. 3. Contoured LOS accelerations. Contours are at 10-mgal intervals, except those notated at Olympus Mons (18°N, 133°W). These accelerations are in addition to a 4th-degree and order background field (*1*). Accelerations are at spacecraft altitudes that were approximately 1000 km at 70°N, 300 km at 25°N, and 1000 km at 30°S.

Condor Chasma, Melas Chasma (5°S, 75°W), and the mouth of Valles Marineris itself (0°, 30°W). There are broad positive anomalies directly associated with Arcadia Planitia (49°N, 14.5°W) and Utopia Planitia (40°N, 225°W).

Near the resolution limits of the data are the large craters such as Cassini (24°N, 328°W) and Antoniadi (21°N, 299°W). Although there are good profiles over these features, the mapping does not show any anomaly associated with them. After some study (*16*), two possible explanations remain: (i) that the craters are very shallow (< 200 m) and therefore have very small anomalies beyond our resolution, or (ii) that they have undergone significant isostatic adjustment. New detailed data on the topographic relief must be obtained before this question can be resolved.

Care must be exercised in the direct application of the numerical values shown in Fig. 3. In addition to the distorting effects mentioned above, there are also the effects of averaging and interpolation in the contouring of the profiles. In many cases, peak variations may never have been sampled as a result of gaps in the data coverage. Moreover, the accelerations due to a 4th-degree and order background field (*1*) have been removed. The maximum effect of the 4th-degree field is an additional 350 mgal at spacecraft altitude in the Tharsis region.

In the second step of the data reduction, quantitative estimates of model masses were sought that would reproduce the data signatures. The approach used was the direct method of fitting to the raw Doppler observations rather than to the LOS profiles (*17*). The reduction proceeded in the following manner. A 2-hour arc of Doppler data that passed over or as near as possible to a feature of interest was selected. An orbit determination program (*18*) having a fixed 4th-degree and order spherical harmonic field (*1*) operated on the data in essentially the same manner as described earlier. However, in this case the masses of approximately ten surface disks (*19*) were estimated in addition to the six components of spacecraft initial position and velocity. One disk whose radius was fixed at the visible feature size was centered at the particular feature of interest whereas the other disks were placed beneath the orbit track at intervals of 10° to 20°, depending on the spacecraft altitude. These nine other disks were used to "absorb" other mass effects that might cause the Doppler residuals to have biases and corrupt the mass estimate of the feature of interest. The Doppler residuals after the fit had a standard deviation of 2 mm/sec (data noise level, ≈ 1 mm/sec), and the sum of the squares of the residuals had been reduced by a factor of 600. Mass estimates for several features are shown in Table 1. The uncertainty in the estimates is approximately 10 percent, and the correlations between adjacent disk masses were less than 0.6.

The average mass estimate of Olympus Mons ($8.7 \pm 0.5 \times 10^{21}$ g) can be compared with estimates obtained from topographic volume estimates and an assumed density of 3.0 g/cm^3. The volume estimates produce masses of 7.8×10^{21} g (*20*) and 6.3×10^{21} g (*21*). These estimates are smaller than the gravity mass estimate and suggest that Olympus Mons has not undergone any isostatic adjustment. There is also the possibility, if the volume and density are reasonably correct, that denser material lies beneath Olympus Mons. This mass-loading produces a compressive stress of 1.7 kbar (*22*). The other volcanic features listed in Table 1 have mass estimates which are less by a factor of 3 to 4 than that of Olympus Mons. I could not find in the literature estimates of volume for these features, except for Arsia Mons (*21*) for which an assumed density of 3.0 g/cm produced a mass of 2.8×10^{21} g.

The Isidis mascon has a mass and size very similar to the lunar mascon in Mare Humorum [5.1×10^{20} g (*23*)]. A possible scenario for its formation is that Isidis Planitia was once a very deep impact basin that underwent considerable isostatic adjustment during a period when Mars was much warmer. Much later (~ 10^9 years), when the crust was thicker and more rigid, erosional deposits accumulated in the basin. Essentially no additional isostatic adjustment occurred at this later time, and the present anomaly exists as a result of Moho relief with only a modest depression in the crust.

The impact of these results on the present geophysical interpretation (*24*) of martian internal structure should be significant. The feature resolution of earlier measurements was very broad and revealed only the most global variations. Now areas such as Olympus Mons, Elysium, and the Isidis basin have very different locations on a plot of observed gravity versus the gravitational equivalent of topography [figure 1 in (*24*)]. These features are no longer in the two populations encompassed by the narrow ellipsis of (*24*) and will require modified explanations to justify their existence in present internal structure models. For example, the theoretical surface gravity is 1200 mgal for the simplified disk model of Olympus Mons presented in Table 1. This essentially uncompensated 600-km feature produces kilobar stresses that demand a thick rigid lithosphere, or some rather unique scenario about very young topography obtained on a presently seismically inert planet.

A gravity contour map over most of the northern hemisphere of Mars has revealed new anomalies directly associated with such visible topography as Olympus Mons, Alba Patera, Ascraeus Mons, Pavonis Mons, Arsia Mons, Elysium Mons, Valles Marineris, and Isidis Planitia. The larger craters, Cassini and Antoniadi, produced no detectable variations. The very large Olympus Mons anomaly should have a very significant impact on geophysical modeling. Similarly, the Elysium anomaly and the Isidis mascon should place constraints on internal structure. Gravity in the southern hemisphere of Mars remains poorly resolved; the anticipated acquisition of Viking Orbiter 1 radio-tracking data in September and October 1978 should extend the 500-km resolution to 40°S.

WILLIAM L. SJOGREN
Jet Propulsion Laboratory,
California Institute of Technology,
Pasadena 91103

References and Notes

1. J. F. Jordan and J. Lorell, *Icarus* **25**, 146 (1975). A 4th-degree and order field was included in the raw data fit because the Doppler data could not be fitted to a level where the high-frequency effects could be seen directly in the residuals (that is, large systematic nonlinear biases overshadowed the gravity anomalies). Since the line-of-sight accelerations were derived in this manner and it is not clear that a direct addition of the 4th-degree and order acceleration is the correct presentation, the line-of-sight accelerations are shown without the background field.
2. W. L. Sjogren, J. Lorell, L. Wong, W. Downs, *J. Geophys. Res.* **80**, 2899 (1975); R. D. Reasenberg, *ibid.* **82**, 369 (1977).
3. J. P. Gapcynski, R. H. Tolson, W. H. Michael, *ibid.*, p. 4325; E. J. Christensen and B. G. Williams, *J. Guidance Control AIAA*, in press.
4. W. L. Sjogren, R. N. Wimberly, D. L. Cain, J. P. Brenkle, *Proc. 9th Lunar Planet. Sci. Conf.*, in press.
5. The orbital parameters are as follows: semimajor axis, 20,028 km; eccentricity, 0.8158; inclination to the true martian equator, 80.3°; period, 24 hours.
6. P. M. Muller and W. L. Sjogren, *Science* **161**, 680 (1968).
7. W. L. Sjogren, R. N. Wimberly, W. R. Wollenhaupt, *Moon* **9**, 115 (1974).
8. P. A. Laing, *"Planetary orbiter error analysis study program (POEAS)"* (Report DUK-5127-OP, Jet Propulsion Laboratory, Pasadena, Calif., 1978) (JPL internal document).
9. An a priori error of 20 km was assigned to each position component to assure convergence, because the short data arc by itself produces a singular information matrix. The a priori uncertainties are larger by several sigmas than those reported by the navigation team who produced the initial state vectors using long data arcs.
10. A circulation of the planet is made every 39 days (the spacecraft orbital period is ≈ 24 hours, and Mars rotates once every 24.62 hours). After a circulation, the orbital tracks fall between those of the previous circulation, providing new coverage between the 9.1° spacing of orbital tracks. Periapsis latitude moves south at ≈ 4.3° per circulation.
11. P. Gottlieb, *Radio Sci.* **5**, 301 (1970).
12. W. L. Sjogren, R. N. Wimberly, W. R. Wollenhaupt, *Moon* **11**, 41 (1974).
13. Atlas of Mars, 1:25,000,000, Topographic Series, M 25M 3MRC, 1976, I-961.

14. A mascon is a positive gravity anomaly located in a topographic depression. They were first discovered on the moon and are associated with circular basins > 200 km in diameter.
15. There is a possibility that one exists under the polar cap but it would be difficult to prove even with low-altitude data.
16. A simulation was performed which indicated that a crater 500 m deep with a diameter of Antoniadi would have produced a LOS acceleration of 10 mgal. This would be easily observed in the data.
17. R. J. Phillips, W. L. Sjogren, E. A. Abbott, S. Zisk, *J. Geophys. Res.*, **83** 5455 (1978).
18. T. D. Moyer, "Mathematical formulation of the double precision orbit determination program (DPODP)" (Report TR 32-1527, Jet Propulsion Laboratory, Pasadena, Calif., 1971).
19. Disks were infinitely thin ellipsoids with no surface curvature. Their centers were placed at a 3393-km radius from the center of gravity. Only ten disks near the orbit were used, for disks farther away would be secondary and highly correlated with the primary ones. The mass solution for a particular feature was derived from the one orbit that passed nearest the feature. Simultaneous solutions based on the use of all orbits with hundreds of surface masses have not been carried out as of this date.
20. M. R. Carr, *J. Geophys. Res.* **78**, 4049 (1973).
21. K. R. Blasius and J. A. Cutts, *Proc. 7th Lunar Sci. Conf.*, (1976), p. 3561.
22. The pressure $p = Mg/A$, where the mass $M = 8.7 \times 10^{21}$ g, the gravitational acceleration $g = 372$ cm/sec^2, 10^6 dyne/cm^2 = 1 bar, and $A = 2/3\ \pi r^2$ (where the radius $r = 6 \times 10^7$ cm and the 2/3 factor is used to account for the disk being an ellipsoid and not a uniform plate and the actual feature is conical). The mass value of 8.7×10^{21} g is considerably larger than what one would obtain by directly using the results in Fig. 3. For example, a point mass estimate would be 4.0×10^{21} g, based on the simple expression $\Delta M = \Delta g r^2/G = (0.3)\ (3 \times 10^7)^2/6.67 \times 10^{-8}$. For a disk the expression is somewhat more complicated but the result, for the same 300-mgal Δg and 300-km altitude, produces 5.9×10^{21} g. This estimate is 32 percent lower than the direct fit result and is consistent with the earlier statement that the least-squares filtering effect reduces the true acceleration amplitude by 30 percent.
23. W. L. Sjogren and W. R. Wollenhaupt, *Moon* **8**, 25 (1973).
24. R. J. Phillips and R. S. Saunders, *J. Geophys. Res.* **80**, 2893 (1975).
25. I thank J. Brenkle of the radio science team for his relentless efforts to acquire data. He even obtained Spaceflight Tracking and Data Network (STDN) tracking when the Deep Space Network station was shut down for modification. I thank G. Cowdrey for compiling the data tapes, E. Klumpe for plotting the data coverage, Z. Shippony for determining the initial conditions of orbit, and B. Wood for his efforts with the STDN tracking network. I thank the host of Deep Space Network operations personnel who made special efforts to ensure the success of this experiment. I especially thank R. Wimberly for his gigantic efforts in the data reduction. I am indebted to A. Ferrari, R. Phillips, M. Ananda, and B. Bills for their comments and review of this report. The research described in this paper was carried out by the Jet Propulsion Laboratory, California Institute of Technology, under NASA contract NAS7-100. This is Jet Propulsion Laboratory planetology publication No. 315-78-05 (JPL internal document).

11 September 1978; revised 1 December 1978

The Estuarine Surface Microlayer and Trace Metal Cycling in a Salt Marsh

Abstract. *The aqueous surface microlayer in a Delaware salt marsh carries an average of 10 percent of the copper, 19 percent of the zinc, and 23 percent of the iron relative to the total metal flux including the dissolved and seston components. Such trace metals cycle in the salt marsh by net import on the surface microlayer and net export in the dissolved and seston components during maximum monthly tides.*

Salt marshes represent an important interface between the land and the sea (*1*), and those dominated by the macrophyte *Spartina alterniflora* are foci for intense biological activity (*2*). Although nutrients and dissolved organic carbon are important exported elements (*3, 4*), the salt marsh also seems to be a source for dissolved and particulate organic materials such as those that collect at the surface microlayer (*5*). A surface microlayer resides on top of most natural bodies of water, and normally it is enriched in organic and metal-bearing materials (*6, 7*). Moreover, the surface microlayer appears to be a source of atmospherically mobilized aerosols through turbulent bubble fractionation (*8*). However, the surface microlayer is a complex region whose thickness (typically less than 100 μm) changes in response to environmental conditions and whose composition comprises a collection of hydrophobic or surface-active materials, particulates, and even biological organisms (*9*). Often the surface microlayer is operationally defined depending on the mode of collection with devices such as meshes, activated drums, or booms.

We examine here the tidal budgets of the trace metals copper, zinc, and iron, carried as (i) dissolved, (ii) particulate, and (iii) microlayer components fluxing in and out of a salt marsh with the tides. One can evaluate the capacity of the surface microlayer to concentrate and transport trace metals in a salt marsh by collecting and analyzing dissolved and seston materials separated by filtration, together with the total surface microlayer. These three sample types (water, seston, and surface microlayer) were gathered periodically over both ebbing and flooding tides in Canary Creek Marsh, Lewes, Delaware (Fig. 1) in the spring, summer, and fall of 1975 at the terminus of the marsh (Pilot Town Road). Canary Creek salt marsh is relatively undisturbed and quite typical of those salt marshes bordering many estuaries and bays of the U.S. East Coast.

Water samples were collected with an uncontaminating plastic pole with a bottle opening at depth and filtered through 0.3-μm, acid-washed glass fiber filters. We analyzed the samples for dissolved trace metals, using ammonium pyrrolidine dithiocarbamate as a chelating agent and methyl isobutyl ketone for solvent extraction (*10*). The water extracts were dried and then digested with hot nitric acid. The surface microlayer was collected during tidal flows with an acid-cleaned, V-shaped polyvinyl chloride boom (*7*), which acts to rapidly collapse hydrophobic and particulate material associated with the surface microlayer at its apex in convenient, water-free gram-size quantities. Solid samples of freeze-dried microlayer material and filtered seston were dried at 75°C and leached with hot nitric acid. All nitric acid digests were made to a constant volume and analyzed by atomic absorption spectrophotometry.

We calculated the trace metal budgets for the marsh (*11*) from the integrated mass of the water multiplied by the trace metal concentrations in the water, seston, and surface microlayer materials collected periodically over the tidal cycle. We monitored the salt marsh only during maximum monthly tides so as to consistently sample during periods of complete inundation and flushing of the marsh. The amount of freshwater drainage in Canary Creek during the sampling periods was negligible, with total salinity excursions of less than 3 per mil. During sampling times, the marsh is assumed to be flooded with the measured quantity of water and seston to greater than 98 percent of its area, which is covered with a uniform surface microlayer to an average thickness of 1.5 μm. The thickness of the surface microlayer is extremely difficult to quantify in situ under all sampling conditions; we judged it on several occa-

Table 1. Trace metal concentrations at the mouth of the Canary Creek salt marsh, averaged over the spring, summer, and fall of 1975; ppb, parts per billion.

Averages for the tidal cycle	Copper (ppb)	Zinc (ppb)	Iron (ppb)
Water, flood	1.2 ± 0.07	1.3 ± 0.07	14.3 ± 0.8
Water, ebb	1.3 ± 0.08	1.6 ± 0.08	39.0 ± 2.0
Microlayer, flood	14,800	103,400	13.9×10^6
Microlayer, ebb	13,800	90,400	15.4×10^6
Particulate, flood (39.4 mg/liter)	37,200	169,000	20.1×10^6
Particulate, ebb (65.4 mg/liter)	26,000	139,000	18.4×10^6